High-Precision Automated 3-D Assembly With Attitude Adjustment Performed by LMTI and Vision-Based Control

Fei Shen, Wenrong Wu, Dahai Yu, De Xu, *Senior Member, IEEE*, and Zhiqiang Cao, *Senior Member, IEEE*

***Abstract*—In this paper, a fully automated microassembly methodology is proposed to assemble a slice micropart into a groupware in three-dimensional (3-D) space with the requirement of attitude adjustment. To accurately acquire the attitude of the slice micropart, we proposed an automated measurement method based on a laser triangulation measurement instrument (LTMI) guided by microscopic vision as well as an accurate calibration method for the telecentric vision system based on nonlinear damping least square method. To achieve automatic assembly, a three-stage microassembly strategy is presented: 1) attitude adjustment of the groupware based on multimicroscopic vision regarding the slice micropart's attitude as the target; 2) coarse-to-fine alignment of the slice micropart to the groupware in 3-D space on the basis of LTMI and microscopic vision; 3) remove microgripper of slice micropart until it is completely glued. Fully automated microassembly experiments are conducted, and the results demonstrate the reasonability of proposed approaches. The task has been performed with the following accuracy: 3 μm for the center position error, 2 μm for the depth error and 0.3° for the attitude error.**

***Index Terms*—Attitude measurement, microassembly, multimicroscopic vision control, telecentric lens calibration, three-dimensional (3-D) alignment.**

I. Introduction

MICROMANIPULATION and microassembly are one of the key techniques in the domain of advanced manufacturing, which can be widely applied to the fields of precision photoelectronic engineering, biotechnology, medical science, microelectromechanism system (MEMS), etc. [1], [2]. On account of the characteristics of tiny object operation and high precision demands, manual operation cannot satisfy the requirement anymore and thus micromanipulation and microassembly robots are needed [3], [4]. Micromanipulation is defined to be high-precision operations (micron accuracy or higher) implemented by the end tools of the robot within a minor work space (centimeter scale or smaller), by virtue of microsensing techniques such as microscopic vision. Moreover, microassembly can be considered as sequences of micromanipulation with the objective of assembling microparts together, which can be further classified into parallel assembly and serial assembly. Compared to parallel assembly, serial assembly has much lower efficiency. However, serial assembly is more suited for the production of complex microsystem with more functions, for its ability of assembling microparts of varying shapes and types with high precision and flexibility. Thus, automated serial microassembly is regarded as a necessary step toward commercial success in microassembly technology because it can increase the productivity dramatically and lower the cost of MEMS devices [5].

Automated microassembly involves some key technologies such as microactuation technology, design of microgripper, measurement and control of micropart.s position and pose based on microscopic vision, measurement and control of microforce, coordinated control of multiple manipulators, etc. Therein, microscopic vision not only offers essential observation methods for microassembly but improves the automatic level as well. At present, research focus of microscopic vision mainly includes autofocus algorithm, depth information acquisition, vision system calibration, control methods based on microscopic.

Since the depth of field of microscopic vision system is generally low, autofocus is used to acquire clear images automatically. The study of autofocus algorithm mainly concentrates on autofocus evaluation function, which can be further classified into spatial domain function and transform domain function, such as gray variance operator, gray gradient operator, image gray entropy, and energy spectrum focus evaluation function. A thorough review with comparative research of the 18 common focus algorithms is given in [6]. As the microscopic vision technique only provides images of the cross-sectional planes, sensing the full three-dimensional (3-D) workspace is quite challenging for microassembly robots. Currently, the focus/defocus technology [7], linear laser scanning method [8], and stereo vision method [9] are the three major depth information acquisition approaches in microassembly. Comparisons among different approaches are given in [10]. It can be seen that the linear laser scanning method

Manuscript received February 24, 2014; revised August 5, 2014 and June 13, 2014; accepted July 11, 2014. Date of publication September 23, 2014; date of current version August 12, 2015. Recommended by Technical Editor B. Shirinzadeh. This work was supported in part by the National Natural Science Foundation of China under Grant 61227804 and Grant 61105036, in part by the Foundation of Laboratory of Precision Manufacturing Technology CAEP under Grant ZZ14003, and in part by the China Postdoctoral Science Foundation.

F. Shen is with the Laser Fusion Research Center, Chinese Academy of Engineering Physics, Mianyang 621900, China, and also with the Research Center of Precision Sensing and Control, Institute of Automation, Chinese Academy of Sciences, Beijing 100190, China (e-mail: fei.shen@ia.ac.cn).

W. Wu and D. Yu are with the Laser Fusion Research Center and Laboratory of Precision Manufacturing Technology, Chinese Academy of Engineering Physics, Mianyang 621900, China (e-mail: rongwwr@tom.com; 93431590@qq.com).

D. Xu is with the Research Center of Precision Sensing and Control, Institute of Automation, Chinese Academy of Sciences, Beijing 100190, China (e-mail: de.xu@ia.ac.cn).

Z. Cao is with the State Key Laboratory of Management and Control for Complex Systems, Institute of Automation, Chinese Academy of Sciences, Beijing 100190, China (e-mail: zhiqiang.cao@ia.ac.cn).

Color versions of one or more of the figures in this paper are available online at http://ieeexplore.ieee.org.

Digital Object Identifier 10.1109/TMECH.2014.2354261

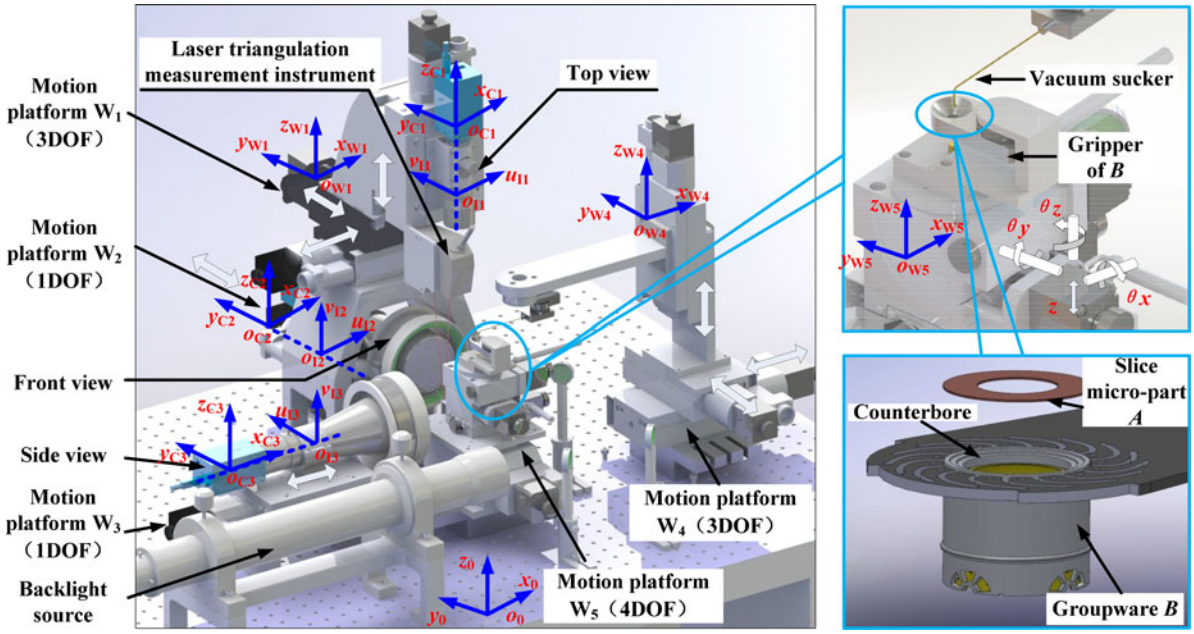

Fig. 1. Structure of microassembly robot system and its coordinate systems.

is aided by lasers and vision to measure the depth, which has the characteristics of high precision and high speed.

When it comes to the attitude measurement of micropart, few achievements have been developed due to the microscopic vision's low depth of field and limited field of view. Among the achievements, Li *et al.* [11] proposed a pose measuring method for the hole on a microsphere and a glass tube using two microscopes with the accuracy of 0.5°. The work developed by Tamadazte *et al.* [12] is also impressing, in which the 3-D poses of the MEMS is supplied by a model-based tracking algorithm in real time with the precision of 0.2°. However, this method relies on the prior CAD model of microparts. In addition, Ma *et al.* [13] proposed a 3-degree-of-freedom (DOF) attitude measuring method using linear variable differential transformers to adjust the relation of position and attitude between the spherical mirror and the resonator.

Besides, it is essential to find the transformation relationship between the visual coordinate system and the measurement coordinate system or manipulator coordinate system, when using the microscopic vision for measurement and control, which is the calibration problem. The calibration methods are mainly classified into photographic measurement method and self-calibration method, just as in the macroscopic field [14]. In the available calibration methods, the pinhole model is generally adopted when establishing the camera model. However, it is not suited to be used for the calibration of widely used microscopic vision system with telecentric lens, which acts as orthographic. Currently, there are few achievements aiming to settle this problem, thus a more accurate model and calibration method are needed.

The development of microscopic vision technology lays a foundation for microassembly automation, based on which many achievements have been attained recently. Wang *et al.* adopted coarse-fine control strategy to perform 3-D automatic grasping of MEMS based on microscopic vision [5], [15]. Tamadazte *et al.* [16] presented the multiscale visual servo control method to automatically grab and assemble silicon devices on the basis of image. Tamadazte *et al.* also proposed a CAD model-based visual servo control method to assemble two kinds of silicon devices [12], [17]. Ferreira *et al.* [18] realized the automated assembly of complex hybrid MEMS devices based on integration of visual force/position servo and virtual reality. Enikov *et al.* [19] employed image-based visual servo control method combined with laser and position sensors to successively put the nickel devices into an array of microslots. Lee *et al.* [20] proposed a global path planning method to consider obstacle avoidance and occlusion rejection in microassembly with an active vision system, which is equipped with a rotational mirror system for changing the viewing direction. Ma *et al.* [13] employed a multisensor control method to realize resonator adjustment for the precise assembly of the optical components.

Although many achievements have been attained in microscopic vision-based microassembly, the following problems still remain unsettled: 1) few research relates to the attitude measurement and control method of micropart; 2) the previous microassembly tasks mainly aim at two-dimensional planes, which are of a little simplicity. Few research concerns the complex 3-D space microassembly, especially those with attitude adjustment.

Aiming at the aforementioned problems, an automatic assembly methodology for a kind of micropart in 3-D space with requirement of attitude adjustment is developed. To acquire the attitude of the slice micropart, an automated measurement method based on a laser triangulation measurement instrument **LTMI** guided by microscopic vision is presented. Meanwhile, a calibration approach for telecentric vision system based on

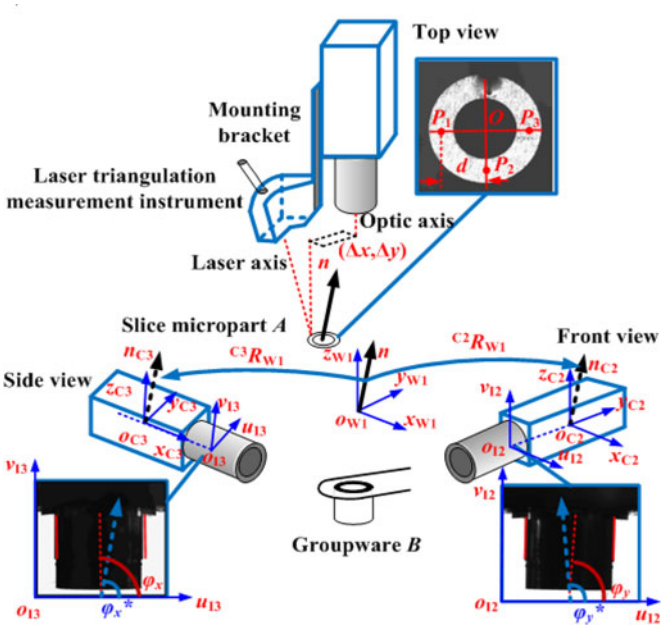

Fig. 2. Schematic of attitude measurement for ***A*** and ***B***.

nonlinear damping least square method is introduced to perform calibrated measurement coordinate systems. To achieve automated assembly for the microparts in 3-D space with high accuracy, a three-stage control strategy is employed. In the first stage, regarding the slice micropart's attitude as the target, attitude adjustment for the groupware is carried out utilizing a servo control method based on multimicroscopic vision. In the second stage, a coarse-to-fine strategy is adopted to align the slice micropart to the counterbore of groupware. The open-loop control is first employed to implement fast coarse alignment and the closed-loop fine alignment for the center of the microparts and the depth difference is carried out subsequently based on microscopic vision and **LTMI**, respectively. In the third stage, after the slice micropart is completely glued, its microgripper is removed to end the assembly. Related assembly experiments are conducted to verify the effectiveness of the proposed methodology.

The rest of the paper is organized as follows. Section II introduces the structure of the microassembly robot system. Section III presents the automated attitude measurement method for microparts and calibration approach for vision system with telecentric lens. Section IV analyzes the control strategy of the entire automated assembly. Section V shows the experiment results and error analysis. Finally, conclusions and suggestions for future work are given in Section VI.

II. Microassembly Robot System and Task Specification

In this paper, a 7-DOF microassembly robot system is utilized to automatically perform 3-D assembly tasks with demand of attitude adjustment as shown in Fig. 1. The complete robot system includes microhandling system, microscopic vision detection system, and master control system.

In the microhandling system, slice micropart ***A*** is absorbed by a vacuum sucker, which is fixed on 3-DOF motion platform $\mathbf{W_4}$. Similarly, groupware ***B*** is absorbed by its gripper that is mounted on the motion platform $\mathbf{W_5}$. Thus, the robot is able to translate ***A*** in three translational DOFs (x, y, and z) and rotate ***B*** in three rotational DOFs (θ_x, θ_y, and θ_z) in combination of one translational DOF (z) simultaneously.

Microscopic vision detection system, designed to measure the position and attitudes of the microparts, consists of a **LTMI** and three microscopic vision systems with their optic axis orthogonal reciprocally named as top view, front view, and side view, respectively. As shown in Fig. 1, each view system is made up of a telecentric lens, a Charge-Coupled Device video camera, and an illuminator. The top-view system is mounted on an independent translational platform $\mathbf{W_1}$ with three DOFs (x, y, and z) while the front- and side-view systems are on translational platform $\mathbf{W_2}$ and $\mathbf{W_3}$ with 1 DOF, respectively. This allows the microscope to be moved independently for auto focus, auto search target, and precise calibration purposes. In addition, to measure the depth information of micropart precisely, a **LTMI** is also fixed on the translational platform $\mathbf{W_1}$. One of the main characteristics of the system is the adoption of telecentric lens, which is suitable to measure the object's edge information profited from its special principle of imaging. On the basis of the information from the microscopic vision detection system, the master system conducts the task by sending control orders to microhandling system where corresponding actions are executed.

Our task in this paper is to utilize the robot to automatically splice a slice micropart ***A***, with thickness of only 30 μm, into the counterbore of the groupware ***B***, which are the key components of a physical laser target used in laser physics experiment. There is a mechanical play of about 50 μm between ***A*** and the counterbore of ***B***. According to the experiment requirement, the position and orientation offset between ***A*** and ***B*** are the key performance indicators. Thus, the solution, including adjustment of the attitude and position alignment, is presented in this paper to meet the requirement mentioned earlier. It should be pointed out that this robot can also be used to assemble other shape of microparts by changing grippers in microhandling system.

In addition, to describe the position and pose of microparts clearly, three categories of frames should be established first, including motor coordinate system, camera coordinate system, and image coordinate system. As shown in Fig. 1, $o_{\mathrm{W}1}x_{\mathrm{W}1}y_{\mathrm{W}1}z_{\mathrm{W}1}$, $o_{\mathrm{W}4}x_{\mathrm{W}4}y_{\mathrm{W}4}z_{\mathrm{W}4}$, and $o_{\mathrm{W}5}x_{\mathrm{W}5}y_{\mathrm{W}5}z_{\mathrm{W}5}$ are the motor coordinate systems attached to motion platform $\mathbf{W_1}$, $\mathbf{W_4}$, and $\mathbf{W_5}$, respectively, with their axes parallel to the stepper motors' moving directions accordingly. $o_{\mathrm{C}1}x_{\mathrm{C}1}y_{\mathrm{C}1}z_{\mathrm{C}1}$, $o_{\mathrm{C}2}x_{\mathrm{C}2}y_{\mathrm{C}2}z_{\mathrm{C}2}$, and $o_{\mathrm{C}3}x_{\mathrm{C}3}y_{\mathrm{C}3}z_{\mathrm{C}3}$ are labeled as camera coordinate systems of the top-, front-, and side-view systems, respectively, whose optic axes coincide with $o_{\mathrm{C}1}z_{\mathrm{C}1}$, $o_{\mathrm{C}2}y_{\mathrm{C}2}$, and $o_{\mathrm{C}3}x_{\mathrm{C}3}$ correspondingly. $o_{\mathrm{I}1}u_{\mathrm{I}1}v_{\mathrm{I}1}$, $o_{\mathrm{I}2}u_{\mathrm{I}2}v_{\mathrm{I}2}$, and $o_{\mathrm{I}3}u_{\mathrm{I}3}v_{\mathrm{I}3}$ are image coordinate systems of the top-, front-, and side-view systems, respectively. $o_{\mathrm{I}1}u_{\mathrm{I}1}$, $o_{\mathrm{I}1}v_{\mathrm{I}1}$, $o_{\mathrm{I}2}u_{\mathrm{I}2}$, $o_{\mathrm{I}2}v_{\mathrm{I}2}$, and $o_{\mathrm{I}3}v_{\mathrm{I}3}$ are parallel to $o_{\mathrm{C}1}x_{\mathrm{C}1}$, $o_{\mathrm{C}1}y_{\mathrm{C}1}$, $o_{C2}x_{\mathrm{C}2}$, $o_{\mathrm{C}2}z_{\mathrm{C}2}$, and $o_{\mathrm{C}3}z_{\mathrm{C}3}$, respectively.

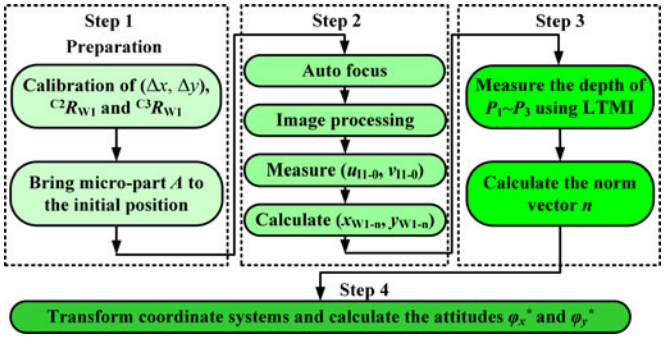

Fig. 3. Flowchart of an automated measurement method for the slice micropart based on **LTMI** guided by microscopic vision.

III. Attitude Measurement Method for Micropart

A. Automated Attitude Measurement Method Based on LTMI Guided by Microscopic Vision

According to the principle of attitude measurement, attitude is generally characterized by the normal vector of feature plane or vector of feature line. As for the microobject with regular shape, the pose vector can be obtained by choosing some corresponding feature points from clear microscopic image. However, as for the slice micropart $\boldsymbol{A}$ with a thickness of only 30 μm but a diameter of 3 mm, when it appears to be an arbitrary posture in the space, clear microscopic image is hard to be obtained due to limited depth of field. Thus, the precise pose vector cannot be gotten. An indirect solution is to measure the pose of the vacuum sucker, connected to $\boldsymbol{A}$, as shown in Fig. 1, whose feature edge information can be obtained precisely. However, since the end surface of vacuum sucker is not very smooth due to the machining error, the posture relationship between the vacuum sucker and the micropart $\boldsymbol{A}$ may vary inevitably among different grasping experiments. This may cause attitude measurement error, which is not acceptable.

In consideration of the error caused by this indirect solution, a direct measurement solution, shown in Fig. 2, is proposed to determine the pose of $\boldsymbol{A}$ by the spatial coordinates of three points P_1, P_2, and P_3 on $\boldsymbol{A}$'s upper surface which are not on a line. Specifically, the normal vector of upper surface $\boldsymbol{n}$, representing the pose of $\boldsymbol{A}$, can be calculated by plane equation determined by the three points. Following this solution, it needs to precisely measure the spatial coordinates of the three points. In this case, **LTMI** based on linear laser scanning method is employed to measure the depth information. In addition, as shown in Fig. 2, the achievement of measuring $\boldsymbol{B}$'s pose can be realized by detecting its edge contour line from the front- and side-view systems. Furthermore, an automated method guided by top view is employed to perform the task of measuring the pose of $\boldsymbol{A}$ and can be divided into four steps shown in Fig. 3.

Step I: Preparation

Since an install location relationship exists between the **LTMI** and the top-view system, as shown in Fig. 2, the deviation between laser axis center and optic axis center of the top-view system, denoted as (Δx, Δy), should be calibrated before automated measurement. In addition, the rotation transform matrices ${}^{\mathrm{C2}}\boldsymbol{R}_{\mathrm{W1}}$ and ${}^{\mathrm{C3}}\boldsymbol{R}_{\mathrm{W1}}$, which represent the posture relationships between the motor frame $\boldsymbol{o}_{\mathrm{W1}}\boldsymbol{x}_{\mathrm{W1}}\boldsymbol{y}_{\mathrm{W1}}\boldsymbol{z}_{\mathrm{W1}}$ and camera frames $\boldsymbol{o}_{\mathrm{C2}}\boldsymbol{x}_{\mathrm{C2}}\boldsymbol{y}_{\mathrm{C2}}\boldsymbol{z}_{\mathrm{C2}}$ and , respectively, need to be calibrated as well. Note that both calibrations only need to be carried out once. Then, $\boldsymbol{A}$ is brought into the field of view of the top-view system.

Step II: Measurement of the plane coordinates of P_1-P_3 in $\boldsymbol{o}_{\mathrm{W1}}\boldsymbol{x}_{\mathrm{W1}}\boldsymbol{y}_{\mathrm{W1}}\boldsymbol{z}_{\mathrm{W1}}$ using top view.

In this step, the top-view system translates in the axis $\boldsymbol{o}_{\mathrm{W1}}\boldsymbol{z}_{\mathrm{W1}}$ direction to focus on $\boldsymbol{A}$ in the pursuit of getting a clear image first. At this moment, the position of the microscope in $\boldsymbol{o}_{\mathrm{W1}}\boldsymbol{x}_{\mathrm{W1}}\boldsymbol{y}_{\mathrm{W1}}\boldsymbol{z}_{\mathrm{W1}}$ is labeled as $(x_{\mathrm{W1-0}}, y_{\mathrm{W1-0}}, z_{\mathrm{W1-0}})$. Then, after some image processing, including denoising and Hough transform, the image coordinates of $\boldsymbol{A}$'s center O denoted as $(u_{\mathrm{I1-0}}, v_{\mathrm{I1-0}})$ is obtained. Since the depth of P_1-P_3 are designed to be measured by **LTMI** and guided by top-view system, their plane coordinates are defined as the position of laser axis center in $\boldsymbol{o}_{\mathrm{W1}}\boldsymbol{x}_{\mathrm{W1}}\boldsymbol{y}_{\mathrm{W1}}\boldsymbol{z}_{\mathrm{W1}}$ when laser axis is on P_n. Hence, the plane coordinates of P_1-P_3 are calculated as

$$x_{\mathrm{W1-n}} = x_{\mathrm{W1-0}} + u_{\mathrm{I1-0}} * \delta + \Delta x + x_{gn}, \quad n = 1, 2, 3 \quad (1)$$

$$y_{\mathrm{W1-n}} = y_{\mathrm{W1-0}} + v_{\mathrm{I1-0}} * \delta + \Delta y + y_{gn}, \quad n = 1, 2, 3 \quad (2)$$

where δ denotes the pixel equivalent which represents the scaling between pixel and the world unit in $\boldsymbol{o}_{\mathrm{W1}}\boldsymbol{x}_{\mathrm{W1}}\boldsymbol{y}_{\mathrm{W1}}\boldsymbol{z}_{\mathrm{W1}}$; (x_{gn}, y_{gn}), named as the guiding coordinates of P_n with a restriction that the three points are not on a line, can be set separately as $(-d, 0)$, $(0, d)$, and $(d, 0)$; d is the distance from center O to P_n, which is preset in advance. The value of d is in the range of (r_1, r_2), where r_1 and r_2 are the radii of inner circle and outer circle of $\boldsymbol{A}$, respectively.

Step III: Measurement of the depth of P_1-P_3 using **LTMI** guided by top-view system and calculate the norm vector $\boldsymbol{n}$.

According to the plane coordinates of P_1-P_3 obtained in the previous step, the laser axis center of **LTMI** can be moved to the target point of P_n to measure its depth, denoted as $\boldsymbol{z}_{\mathrm{W1-n}}$, by translating the axis $\boldsymbol{o}_{\mathrm{W1}}\boldsymbol{x}_{\mathrm{W1}}$ and $\boldsymbol{o}_{\mathrm{W1}}\boldsymbol{y}_{\mathrm{W1}}$ of $\mathbf{W}_1$. Hence, based on the three target points' spatial coordinates, the normal vector of upper surface $\boldsymbol{n}$ can be calculated as

$$\begin{aligned}\boldsymbol{n} &= \overrightarrow{P_2P_1} \times \overrightarrow{P_2P_3} = [\, n_x \quad n_y \quad n_z \,]^T \\ &= \begin{bmatrix} (z_{\mathrm{W1-3}} - z_{W1-2})(y_{\mathrm{W1-2}} - y_{W1-1}) \\ -(z_{\mathrm{W1-2}} - z_{\mathrm{W1-1}})(y_{\mathrm{W1-3}} - y_{\mathrm{W1-2}}) \\ (z_{\mathrm{W1-2}} - z_{\mathrm{W1-1}})(x_{\mathrm{W1-3}} - x_{\mathrm{W1-2}}) \\ -(z_{\mathrm{W1-3}} - z_{\mathrm{W1-2}})(x_{\mathrm{W1-2}} - x_{\mathrm{W1-1}}) \\ (y_{\mathrm{W1-3}} - y_{\mathrm{W1-2}})(x_{\mathrm{W1-2}} - x_{\mathrm{W1-1}}) \\ -(y_{\mathrm{W1-2}} - y_{\mathrm{W1-1}})(x_{\mathrm{W1-3}} - x_{\mathrm{W1-2}}) \end{bmatrix}\end{aligned} \quad (3)$$

where n_x, n_y, and n_z are the components of normal vector $\boldsymbol{n}$.

Step IV: Transformation of the coordinate systems

As shown in Fig. 2, the normal vector $\boldsymbol{n}$ of $\boldsymbol{A}$ obtained in the previous step is represented in $\boldsymbol{o}_{\mathrm{W1}}\boldsymbol{x}_{\mathrm{W1}}\boldsymbol{y}_{\mathrm{W1}}\boldsymbol{z}_{\mathrm{W1}}$, while the attitudes of $\boldsymbol{B}$ are measured directly in the image frames of $\boldsymbol{o}_{\mathrm{I2}}\boldsymbol{u}_{\mathrm{I2}}\boldsymbol{v}_{\mathrm{I2}}$ and $\boldsymbol{o}_{\mathrm{I3}}\boldsymbol{u}_{\mathrm{I3}}\boldsymbol{v}_{\mathrm{I3}}$. Thus, in order to unify the description, the rotation transform matrices ${}^{\mathrm{C2}}\boldsymbol{R}_{\mathrm{W1}}$ and ${}^{\mathrm{C3}}\boldsymbol{R}_{\mathrm{W1}}$ are employed to transform $\boldsymbol{n}$ into $\boldsymbol{n}_{\mathrm{C2}}$ and $\boldsymbol{n}_{\mathrm{C3}}$, which are

represented in $\boldsymbol{o_{C2}x_{C2}y_{C2}z_{C2}}$ and $\boldsymbol{o_{C3}x_{C3}y_{C3}z_{C3}}$, respectively, and calculated as

$$\boldsymbol{n_{C2}} = {}^{\mathbf{C2}}\boldsymbol{R_{W1}} \cdot \boldsymbol{n} = [\, n_{xC2} \quad n_{yC2} \quad n_{zC2} \,]^T \tag{4}$$

$$\boldsymbol{n_{C3}} = {}^{\mathbf{C3}}\boldsymbol{R_{W1}} \cdot \boldsymbol{n} = [\, n_{xC3} \quad n_{yC3} \quad n_{zC3} \,]^T \tag{5}$$

where n_{xC2}, n_{yC2}, and n_{zC2} are the components of normal vector $\boldsymbol{n_{C2}}$; n_{xC3}, n_{yC3}, and n_{zC3} are the components of $\boldsymbol{n_{C3}}$. Hence, the attitudes denoted as φ_x^* and φ_y^*, projection of the normal vector $\boldsymbol{n}$ on $\boldsymbol{o_{I2}u_{I2}v_{I2}}$ and $\boldsymbol{o_{I3}u_{I3}v_{I3}}$, respectively, can be obtained as

$$\varphi_x^* = -\text{atan}\left(\frac{n_{xC2}}{n_{zC2}}\right) + \frac{\pi}{2} \tag{6}$$

$$\varphi_y^* = -\text{atan}\left(\frac{n_{yC3}}{n_{zC3}}\right) + \frac{\pi}{2} \tag{7}$$

where $\pi/2$ is an offset because the attitudes' baseline are selected as the axes $\boldsymbol{o_{I2}u_{I2}}$ and $\boldsymbol{o_{I3}u_{I3}}$, respectively.

So far, we have introduced the proposed attitude measurement method. It can be seen that the measurement accuracy of φ_x^* and φ_y^* may rely on the repeatable accuracy of motion platform, measurement accuracy of **LTMI**, and calibration accuracy of rotation matrix. Despite the first two aspects, the performance of the attitude measurement can be improved by employing a precise calibration method. Since the calibration method for telecentric optical system, which is used in the front- and side-view systems, is rare in the current literature, a precise calibration method based on nonlinear damping least square method will be introduced in the next section.

B. Calibration Method for Telecentric Visual System

Telecentric lenses have the unique properties of purely orthographic projections of scene points and maintaining a constant magnification over a specific range of object distances called as telecentric depth, which is less than the depth of field commonly. Hence, they are ideally suited for precision measuring applications where the position of the object being inspected need not be rigorously defined. In other words, the image magnification in telecentric optical system does not depend on the object distance, which is different from the ordinary optical system.

1) Camera Model of Telecentric Vision System: The complete camera model includes intrinsic parameter model and extrinsic parameter model. Concerning the intrinsic parameter model, the most widely used pin-hole model based on perspective projection is not suited to be used here anymore as the telecentric lenses act as orthographic. According to the work principle of telecentric lenses, the intrinsic parameter model without consideration of lens distortion can be obtained in matrix form as

$$\begin{bmatrix} u \\ v \\ 1 \end{bmatrix} = \begin{bmatrix} k_x & 0 & u_0 \\ 0 & k_y & v_0 \\ 0 & 0 & 1 \end{bmatrix} \begin{bmatrix} x_c \\ y_c \\ 1 \end{bmatrix} (z_c \in [z_0, z_0 + \Delta z]) \tag{8}$$

where (u, v) is the image coordinate and (x_c, y_c, z_c) is coordinate of the scene point represented in the camera coordinate system $\boldsymbol{o_C x_C y_C z_C}$. (u_0, v_0) is the image coordinates of principal point. Δz is telecentric depth and z_0 is the nearest object position with a clear image. k_x and k_y, respectively, are the magnification factor of the x-axis and y-axis directions. Note that (u_0, v_0) is zero for telecentric lenses as it performs parallel projection [21]. Furthermore, due to the improvement of manufacturing technology of isotropic image sensors, the magnification factors along x and y are identical, that is, $k_x = k_y = k$.

Then, the extrinsic parameter model is expressed as

$$\begin{bmatrix} x_c \\ y_c \\ z_c \\ 1 \end{bmatrix} = \begin{bmatrix} r_{11} & r_{12} & r_{13} & \boldsymbol{p}_x \\ r_{21} & r_{22} & r_{23} & \boldsymbol{p}_y \\ r_{31} & r_{32} & r_{33} & \boldsymbol{p}_z \\ 0 & 0 & 0 & 1 \end{bmatrix} \begin{bmatrix} x_w \\ y_w \\ z_w \\ 1 \end{bmatrix} = \begin{bmatrix} \boldsymbol{R} & \boldsymbol{p} \\ 0 & 1 \end{bmatrix} \begin{bmatrix} x_w \\ y_w \\ z_w \\ 1 \end{bmatrix} \tag{9}$$

where (x_w, y_w, z_w) is the coordinate of the scene points in the world coordinate system $\boldsymbol{o_w x_w y_w z_w}$. $\boldsymbol{R}$ and $\boldsymbol{p}$, denoted as the rotation matrix and translation vector, respectively, represent the transform relationship between $\boldsymbol{o_w x_w y_w z_w}$ and $\boldsymbol{o_C x_C y_C z_C}$; r_{11}, r_{12}, r_{13}, r_{21}, r_{22}, r_{23}, r_{31}, r_{32}, r_{33}, p_x, p_y, and p_z are their elements.

Finally, combining (8) and (9), the camera model of the telecentric optical system with matrix form is given as

$$\begin{bmatrix} u \\ v \\ 1 \end{bmatrix} = \begin{bmatrix} k & 0 & 0 \\ 0 & k & 0 \\ 0 & 0 & 1 \end{bmatrix} \begin{bmatrix} r_{11} & r_{12} & r_{13} & p_x \\ r_{21} & r_{22} & r_{23} & p_y \\ 0 & 0 & 0 & 1 \end{bmatrix} \begin{bmatrix} x_w \\ y_w \\ z_w \\ 1 \end{bmatrix}. \tag{10}$$

2) Calibration Method for Telecentric Vision System Based on Nonlinear Damping Least Squares Method: Essentially, the calibration method aims to solve the unknown variables such as r_{11}, r_{12}, etc., in the camera model, which characterize the relationship between coordinate systems. Equation (10) is rewritten as

$$\begin{cases} u = k(r_{11}x_w + r_{12}y_w + r_{13}z_w + p_x) \\ v = k(r_{21}x_w + r_{22}y_w + r_{23}z_w + p_y) \end{cases}. \tag{11}$$

Considering the aforementioned equations, multiple sets of scene points denoted as R_i whose world coordinate and image coordinate are denoted as (x_{wi}, y_{wi}, z_{wi}) and (u_i, v_i), respectively, are then required for the solvent. Moreover, it is noted that the rotation angles between $\boldsymbol{o_w x_w y_w z_w}$ and $\boldsymbol{o_C x_C y_C z_C}$, named as β_x, β_y, and β_z, can be used to express r_{11}, r_{12}, r_{13}, r_{21}, r_{22}, and r_{23} as follows [22]:

$$\begin{aligned} &r_{11} = \cos\beta_z \cos\beta_y, r_{12} = \cos\beta_z \sin\beta_y \sin\beta_x - \sin\beta_z \cos\beta_x \\ &r_{21} = \sin\beta_z \cos\beta_y, r_{22} = \sin\beta_z \sin\beta_y \sin\beta_x + \cos\beta_z \cos\beta_x \\ &r_{13} = \cos\beta_z \sin\beta_y \cos\beta_x + \sin\beta_z \sin\beta_x \\ &r_{23} = \sin\beta_z \sin\beta_y \cos\beta_x - \cos\beta_z \sin\beta_x. \end{aligned} \tag{12}$$

Thus, using (11) and knowing the magnification factor k, m sets of sample data can form $2m$ equations with unknown vector $\boldsymbol{x} = (\beta_x, \beta_y, \beta_z, p_x, p_y)$, which are overdetermined nonlinear equations and given by

$$\boldsymbol{f}(\boldsymbol{x}) = \begin{bmatrix} f_1(\beta_x, \beta_y, \beta_z, p_x, p_y) \\ f_2(\beta_x, \beta_y, \beta_z, p_x, p_y) \\ \cdots \\ f_{2m}(\beta_x, \beta_y, \beta_z, p_x, p_y) \end{bmatrix} = 0 \quad (2m > 5) \tag{13}$$

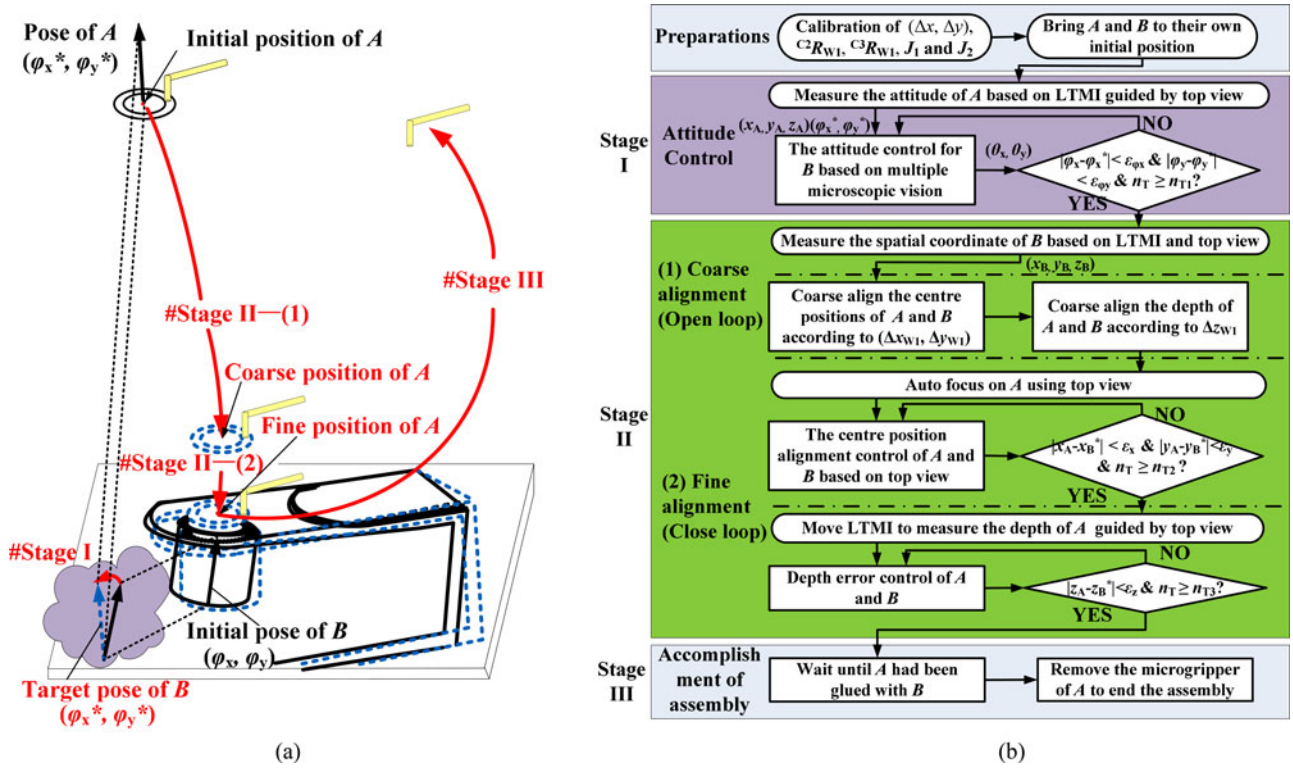

Fig. 4. Schematic and flowchart of automatic assembly (a) the schematic of automated assembly; (b) flowchart of automated assembly.

where $f_i = u_i - k(r_{11}x_{wi} + r_{12}y_{wi} + r_{13}z_{wi} + p_x)$, $f_{2i} = v_i - k(r_{21}x_{wi} + r_{22}y_{wi} + r_{23}z_{wi} + p_y), i = 1, \ldots, m$. To solve the above overdetermined nonlinear equations precisely, it can be translated into a form of quadratic functional $\Phi(\boldsymbol{x})$ as follows:

$$\Phi(\boldsymbol{x}) = \frac{1}{2}\boldsymbol{f}(\boldsymbol{x})^T\boldsymbol{f}(\boldsymbol{x}) = \frac{1}{2}\sum_{i=1}^{2m} f_i^2(x). \tag{14}$$

Hence, the minimum value of function $\Phi(\boldsymbol{x})$ denoted as $\boldsymbol{x}^*$ is the least-squares solution of the overdetermined equations $f(\mathbf{x}) = 0$ and expressed as

$$\Phi(\boldsymbol{x}^*) = \min_{\boldsymbol{x}\in R^n}\Phi(\boldsymbol{x}) = \min_{\boldsymbol{x}\in R^n}\frac{1}{2}\boldsymbol{f}(\boldsymbol{x})^T\boldsymbol{f}(\boldsymbol{x}). \tag{15}$$

Therefore, the solvent of the overdetermined equations can be achieved by searching the minimum value of multifunction $\Phi(\boldsymbol{x})$. If $\boldsymbol{f}(\boldsymbol{x})$ is differential in the domain, the gradient of $\Phi(\boldsymbol{x})$ denoted as $\boldsymbol{g}(\boldsymbol{x})$ is set to be zero as follows:

$$\boldsymbol{g}(\boldsymbol{x}) = \because\Phi(\boldsymbol{x}) = \frac{1}{2}\boldsymbol{D}\boldsymbol{f}(\boldsymbol{x})^T\boldsymbol{f}(\boldsymbol{x}) = 0 \tag{16}$$

where

$$\boldsymbol{D}f(\boldsymbol{x})^T = \begin{bmatrix} \frac{\partial f_1}{\partial \beta_x} & \frac{\partial f_2}{\partial \beta_x} & \cdots & \frac{\partial f_{2m}}{\partial \beta_x} \\ \frac{\partial f_1}{\partial \beta_y} & \frac{\partial f_2}{\partial \beta_y} & \cdots & \frac{\partial f_{2m}}{\partial \beta_y} \\ \vdots & \vdots & & \vdots \\ \frac{\partial f_1}{\partial p_y} & \frac{\partial f_2}{\partial p_y} & \cdots & \frac{\partial f_{2m}}{\partial p_y} \end{bmatrix}.$$

The Taylor's expansion of $\boldsymbol{f}(\boldsymbol{x})$ at the point $\boldsymbol{x}^{\mathbf{k}}$ can be expressed as

$$\boldsymbol{f}(\boldsymbol{x}) \approx \boldsymbol{f}(\boldsymbol{x}^{\mathrm{k}}) + \boldsymbol{D}\boldsymbol{f}(\boldsymbol{x}^{\mathrm{k}})(\boldsymbol{x} - \boldsymbol{x}^{\mathrm{k}}). \tag{17}$$

Substituting the aforementioned equation into (16), the iterative $\boldsymbol{x}$ can be obtained as

$$\boldsymbol{x}^{\mathrm{k}+1} = \boldsymbol{x}^{\mathrm{k}} - \boldsymbol{G}(\boldsymbol{x}^{\mathrm{k}})^{-1}\boldsymbol{D}\boldsymbol{f}(\boldsymbol{x}^{\mathrm{k}})^{\mathrm{T}}\boldsymbol{f}(\boldsymbol{x}^{\mathrm{k}}) \tag{18}$$

where $\boldsymbol{G}(\boldsymbol{x}^{\mathbf{k}}) = \boldsymbol{D}\boldsymbol{f}(\boldsymbol{x}^{\mathbf{k}})^{\mathbf{T}}\boldsymbol{D}\boldsymbol{f}(\boldsymbol{x}^{\mathbf{k}})$ is the iterative matrix. In order to prevent the iterative matrix $\boldsymbol{G}(\boldsymbol{x}^{\mathbf{k}})$ from being singular or pathological, based on Levenberg–Marquardt method one damping item denoted as $\mu_k\boldsymbol{I}$ is added to the iterative matrix [23], which will then become $\boldsymbol{G}'(\boldsymbol{x}^{\mathbf{k}}) = \boldsymbol{D}\boldsymbol{f}(\boldsymbol{x}^{\mathbf{k}})^{\mathbf{T}}\boldsymbol{D}\boldsymbol{f}(\boldsymbol{x}^{\mathbf{k}}) + \mu_k\boldsymbol{I}$. Thus, the new iteration formula is given by

$$\boldsymbol{x}^{\mathrm{k}+1} = \boldsymbol{x}^{\mathrm{k}} - \boldsymbol{G}'(\boldsymbol{x}^{\mathrm{k}})\boldsymbol{D}\boldsymbol{f}(\boldsymbol{x}^{\mathrm{k}})^{\mathrm{T}}\boldsymbol{f}(\boldsymbol{x}^{\mathrm{k}}). \tag{19}$$

Based on the principles mentioned earlier, specific steps for calibrating telecentric optical system are as follows:

1) Sample m sets of scene points R_i with (x_{wi}, y_{wi}, z_{wi}) and (u_i, v_i), and then form $2m$ equations according to (13).
2) Calculate the iterative matrix $G'(\boldsymbol{x}^k)$.
3) Solve the unknown vector $\boldsymbol{x}$ by applying the iteration formula (19). Specifically, the iterative process starts with a selected initial value and stops until the 2-norm of the two adjacent vectors' error becomes smaller than the threshold value. Therefore, following the aforementioned calibration steps, we can get the rotation transform matrices ${}^{\mathbf{C2}}\boldsymbol{R}_{\mathbf{W1}}$ and ${}^{\mathbf{C3}}\boldsymbol{R}_{\mathbf{W1}}$.

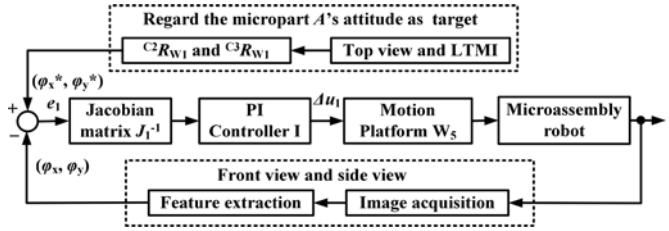

Fig. 5. Attitude control system based on multimicroscopic vision.

IV. Automated Control Method for Microassembly in 3-D Space

Compared to the available automated microassembly tasks, the task presented in this paper is more complicated due to its requirements of both attitude and position alignment precision. Different from the assembly task in the macrodomain, little sorts of sensors can be relied on in microassembly. For the assembly task in this paper, three microscopic vision systems and an **LTMI** are used as sensors.

Based on microscopic vision and **LTMI**, a three-stage automated assembly strategy is presented whose schematic and flowchart are shown in Fig. 4(a) and (b), respectively. The entire assembly task is divided into three stages: 1) attitude adjustment based on multimicroscopic vision; 2) coarse-to-fine alignment control based on microscopic vision and **LTMI**; 3) remove the microgripper of the slice micropart ***A*** after it is completely glued.

It is noticed that two preparations should be carried out manually prior to assembly: 1) calibrate deviation $(\Delta x, \Delta y)$, transform matrices ${}^{\mathbf{C2}}\boldsymbol{R}_{\mathbf{W1}}$, ${}^{\mathbf{C3}}\boldsymbol{R}_{\mathbf{W1}}$, Jacobian matrix $\boldsymbol{J}_1$, and $\boldsymbol{J}_2$ whose function will be introduced in the following part; 2) clamp micropart ***A*** and ***B*** with glue spreading on the lower surface of ***A***, then bring them to the initial positions where ***A*** is in the field view of top-view system and ***B*** is in the public field of front- and side-view systems. Note that the former preparation only needs to be implemented once, while the latter one needs to repeat before each assembly task.

A. Attitude Control Based on Multimicroscopic Visions

The objective of this stage is to adjust the attitude of groupware ***B*** based on the front- and side-view systems. In this stage, as shown in Fig. 4(b), the attitudes and position of micropart ***A***, denoted as $(\varphi_x^*, \varphi_y^*)$ and (x_A, y_A, z_A), respectively, need to be measured first using the method proposed in Section III. Then, regarding ***A***'s attitude as target, the adjustment of ***B***'s attitude is implemented by rotating the axes θ_x and θ_y of $\mathbf{W_5}$. To achieve automated adjustment, an attitude controller based on the front- and side-view systems is presented.

As shown in Fig. 5, the attitude control system mainly includes the Jacobian matrix $\boldsymbol{J}_1$, PI controller I, motion platform $\mathbf{W_5}$, microassembly robot, and front- and side-view systems. The Jacobian matrix $\boldsymbol{J}_1$, described the relationship between the changes of robot joint vector and attitude vector denoted as $\varphi = [\theta_x, \theta_y]$ and $\varphi = [\varphi_x, \varphi_y]$, respectively, can be expressed as $\dot{\boldsymbol{\varphi}} = \boldsymbol{J_1}(\theta)\dot{\theta}$. The inverse Jacobian matrix is employed to estimate the robot joint error vector from the attitude error vector $\mathbf{e}_1$ defined as $\mathbf{e}_1 = [\varphi_x - \varphi_x^* \ \varphi_y - \varphi_y^*]^T$. φ_x and φ_y are the attitudes of ***B*** directly obtained from the front- and side-view systems, respectively, through image acquisition and feature extraction. Note that the Jacobian matrix $\boldsymbol{J}_1$ is obtained off-line and its calibration method is similar to that presented in [24]. Then, the output of the PI controller which is fed into the stepping motor of $\mathbf{W_5}$ is written as

$$\Delta \boldsymbol{u_1}(k) = K_{P1}\boldsymbol{J_1^{-1}}(\boldsymbol{e_1}(k) - \boldsymbol{e_1}(k-1)) + K_{I1}\boldsymbol{J_1^{-1}}\boldsymbol{e_1}(k) \tag{20}$$

where K_{P1} and K_{I1} are proportional and integral coefficients of the PI controller, respectively; $\mathbf{e}_1(k)$ and $\mathbf{e}_1(k-1)$ represent the current attitude error vector and error vector at instant $k-1$, respectively. Therefore, as shown in Fig. 4(b), once the attitude error had been adjusted within specified range with n_{T1} control periods continuously, the assembly process will automatically jump into the stage of coarse-to-fine alignment control.

B. Coarse-to-Fine Alignment Control Based on Microscopic Vision and *LTMI*

The main purpose of this stage is to achieve the alignment of ***A*** and ***B***'s counterbore, requiring that the distance between the lower surface of ***A*** and the upper surface of ***B***'s counterbore meet the gluing demand and their centers of inter circle coincide. In order to achieve rapid and precise alignment, this paper presents a coarse-to-fine control strategy, including coarse alignment of the open-loop control and precise alignment of closed-loop control. The former aims at increasing the speed while the latter ensures the final alignment accuracy.

1) Coarse Alignment Control: Since the center position of ***A***'s inner circle and its depth had been measured and recorded in the previous stage, denoted as $(x_{\mathrm{W1}-A}, y_{\mathrm{W1}-A}, z_{\mathrm{W1}-A})$, it is only necessary to measure ***B***'s position $(x_{\mathrm{W1}-B}, y_{\mathrm{W1}-B}, z_{\mathrm{W1}-B})$. Similar to the measurement method of ***A***, the center coordinates of inner circle is obtained after auto focus and feature extraction, denoted as $(x_{\mathrm{I1}-B}, y_{\mathrm{I1}-B})$. Using the same method for measuring the depth of P_2 on ***A***'s upper surface, the depth of the corresponding point P_2' on the upper surface of ***B***'s counterbore, denoted as $z_{\mathrm{W1}-B}$, is measured automatically by **LTMI** guided by the top-view system.

Thus, regarding the spatial position of ***B*** as target, the control variable $(Dx_{\mathrm{W1}-A}, Dy_{\mathrm{W1}-A}, Dz_{\mathrm{W1}-A})$ is obtained and finally fed into the motion platform $\mathbf{W_4}$, wherein $Dx_{\mathrm{W1}-A} = x_{\mathrm{W1}-A} - x_{\mathrm{W1}-B}$, $Dy_{\mathrm{W1}-A} = y_{\mathrm{W1}-A} - y_{\mathrm{W1}-B}$, and $Dz_{\mathrm{W1}-A} = z_{\mathrm{W1}-A} - z_{\mathrm{W1}-B} - d_A - \delta_A$. Here, d_{A} denotes the thickness of ***A*** and δ_A represents the gap distance between ***A*** and ***B*** where glue is filled with. Since the initial position of ***A*** locates out of ***B***'s counterbore, as shown in Fig. 4(a), in order to avoid collision, the coarse center alignment is implemented by driving the x-axis and y-axis of motion platform $\mathbf{W_4}$ at first, and the coarse depth alignment is carried out followed by driving the z-axis. After the stepper motor driving the z-axis had been arrived at the target in accordance with the control variable, the assembly process will automatically jump into the stage of fine alignment control.

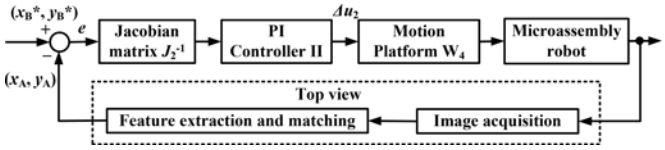

Fig. 6. Center alignment control system based on top-view system.

2) Fine Alignment Control: Since the coarse alignment is an open-loop control process, the alignment error exists inevitably and thus needs to be further compensated in fine alignment. The complete fine alignment has to be divided into center fine alignment and depth alignment due to the center position and depth of $\boldsymbol{A}$ cannot be measured at the same time. For the convenient of measuring, the center alignment is implemented before the depth alignment.

To achieve the center alignment automatically, we present a center fine alignment control system based on top-view system, which includes the Jacobian matrix $\boldsymbol{J}_2$, PI controller II, motion platform $\mathbf{W_4}$, microassembly robot, and the top-view system, as shown in Fig. 6. The Jacobian matrix $\boldsymbol{J}_2$, representing the relationship between the changes of robot joint vector and center position vector denoted as $\boldsymbol{g}_1 = [x_{\mathrm{W4}}, y_{\mathrm{W4}}]$ and $\boldsymbol{g}_2 = [x_{\mathrm{I1}-A}, y_{\mathrm{I1}-A}]$, respectively, can be expressed as $\dot{\boldsymbol{g}}_2 = \boldsymbol{J}_2\boldsymbol{g}_1\dot{\boldsymbol{g}}_1$. The inverse Jacobian matrix $\boldsymbol{J}_2$ is used to compute the robot joint error vector from the center position error vector between $\boldsymbol{A}$ and $\boldsymbol{B}$ defined as $\boldsymbol{e}_2 = [\,x_{\mathrm{I1-A}} - x^*_{\mathrm{I1-B}}\ y_{\mathrm{I1-A}} - y^*_{\mathrm{I1-B}}\,]^T$. Here, $x_{\mathrm{I1}-A}$ and $y_{\mathrm{I1}-A}$ are plane coordinates of $\boldsymbol{A}$'s inner circle center obtained from the top-view system through image acquisition, feature extraction, and matching.

Thus, the output of the PI controller which is fed into the stepping motor to drive the x-axis and y-axis of the motion platform $\mathbf{W_4}$ is written as

$$\Delta\boldsymbol{u}_2(k) = K_{P2}\boldsymbol{J}_2^{-1}(\boldsymbol{e}_2(k) - \mathbf{e}_2(k-1)) + K_{\mathrm{I2}}\boldsymbol{J}_2^{-1}\boldsymbol{e}_2(k) \tag{21}$$

where K_{P2} and K_{I2} are the proportional and integral coefficients of PI controller II, respectively; $e_2(k)$ and $e_2(k\text{-}1)$ represent the current center position error and center position error at instant k-1 accordingly.

Therefore, as shown in Fig. 4(b), as soon as the center position error had been reduced within specified range with n_{T2} control periods continuously, the depth fine alignment based on **LTMI** will be carried out in the next. Before the depth alignment, **LTMI** needs to be guided by the top-view system to measure the depth of the point P_2' on the upper surface of $\boldsymbol{A}$, which is denoted as $z_{\mathrm{W1}-A}$. Regarding the depth $z_{\mathrm{W1-A}} = z_{\mathrm{W1-b}} - d_A - \delta_A$ as target, a PID controller III based on **LTMI** is employed to realize the depth fine alignment. The input of the controller is the depth error defined as $e_3 = z_{\mathrm{W1-A}} - z^*_{\mathrm{W1-A}}$. The output of the PID controller which is fed into the stepper motor for driving the z-axis of motion platform $\mathbf{W_4}$ is obtained as

$$\begin{aligned}\Delta u_3(k) = {} & K_{\mathrm{P3}}\Delta\boldsymbol{e}_3(k) + K_{\mathrm{I3}}\boldsymbol{e}_3(k) + K_{\mathrm{D3}}(\boldsymbol{e}_3(k) \\ & -2\boldsymbol{e}_3(k-1) + \boldsymbol{e}_3(k-2))\end{aligned} \tag{22}$$

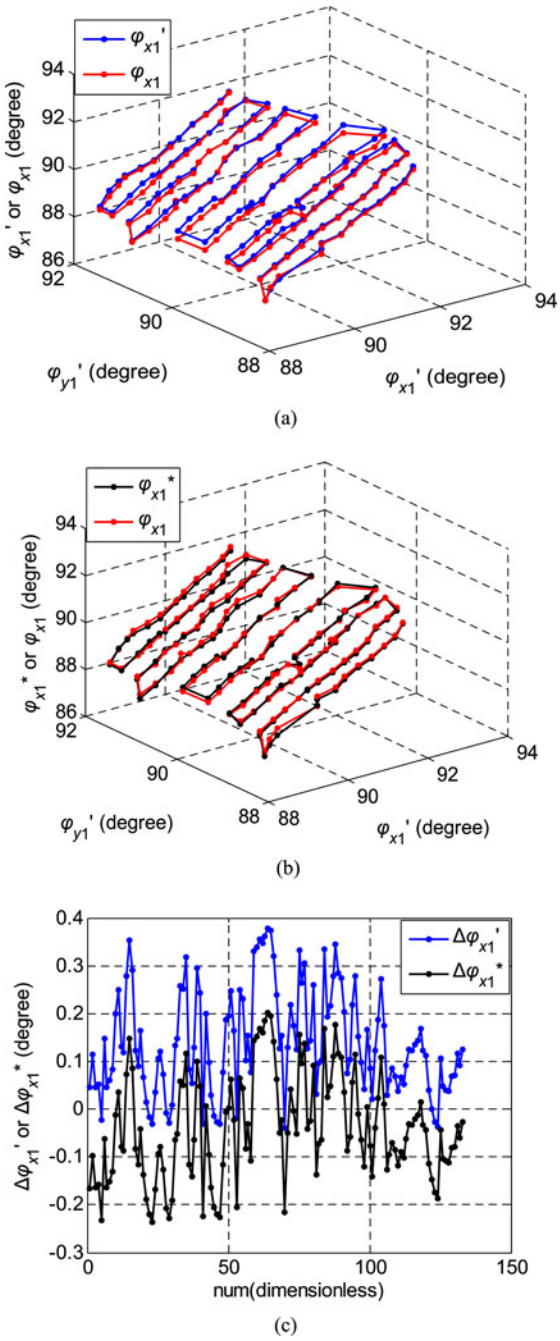

Fig. 7. Results of verified experiment for the calibration method: (a) the contrast measurement results between φ'_{x1} and φ_{x1}; (b) the contrast measurement results between φ^*_{x1} and φ_{x1}; (c) the curves of attitude error $\Delta\varphi'_{x1}$ and $\Delta\varphi^*_{x1}$.

where K_{P3}, K_{I3}, and K_{D3} are the proportional, integral and differential coefficients of PID controller III, respectively. $e_3(k)$, $e_3(k-1)$, $e_3(k-2)$, and $\Delta e_3(k) = e_3(k) - e_3(k-1)$ represent the current depth error, error at instant $k-1$, error at instant $k-2$, and error change, respectively.

Similarly, once $\boldsymbol{A}$ had been arrived at the target within a specified depth error range with n_{T3} control period continuously, the assembly process will jump into the stage III automatically. In this stage, after the glue spread on the lower surface of $\boldsymbol{A}$ beforehand had been solidified with $\boldsymbol{B}$ in virtue of ultraviolet

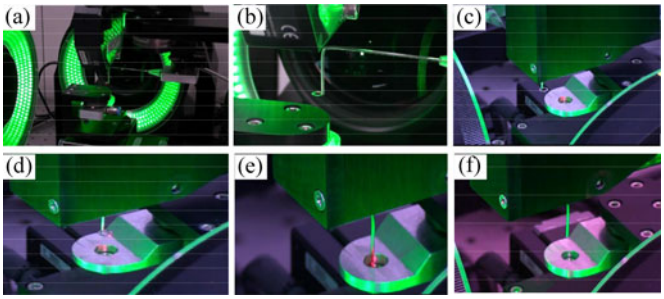

Fig. 8. Sequence snapshots of the automated microassembly.

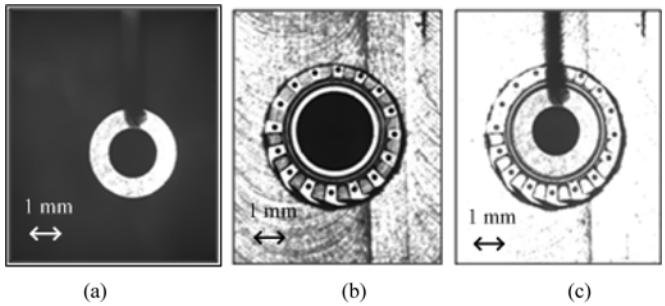

Fig. 9 Images obtained from the top-view system (a) slice micropart ***A***; (b) groupware ***B***; (c) ***A*** and ***B***.

source, the power source of the vacuum pump system in ***A***'s microgripper is turned off and then the microgripper of ***A*** can be removed to end the assembly.

V. Experiments and Analysis

To verify the proposed measurement and control method, a series of experiments were conducted on the microassembly robot.

A. Calibration Results for Telecentric Visual Systems and Verified Experiments

According to the proposed calibration method, a small metal ball with a diameter of 1 mm is used to sample m sets of scene points R_i with (x_{wi}, y_{wi}, z_{wi}) and (u_i, v_i). The small metal ball gluing with a slim tube is mounted on the motion platform $\mathbf{W_1}$. Using eight data sets in the proposed calibration steps, the rotation angles between $\boldsymbol{o_{W1}x_{W1}y_{W1}z_{W1}}$ and $\boldsymbol{o_{C3}x_{C3}y_{C3}z_{C3}}$ as well as the partial translational vector elements are obtained as $\beta_{x3} = 0.16°$, $\beta_{y3} = 1.15°$, $\beta_{z3} = 0.95°$, $p_{y3} = 41.886$ mm, and $p_{z3} = 18.653$ mm. Similarly, the calibration result of the relationship between $\boldsymbol{o_{W1}x_{W1}y_{W1}z_{W1}}$ and $\boldsymbol{o_{C2}x_{C2}y_{C2}z_{C2}}$ are also acquired as $\beta_{x2} = 0.92°$, $\beta_{y2} = 0.048°$, $\beta_{z2} = -1.13°$, $p_{x2} = -32.757$ mm, and $p_{z2} = 17.289$ mm. Note that the translational elements are not further used in this paper. Therefore, the rotation matrices ${}^{\mathbf{C2}}\boldsymbol{R}_{\mathbf{W1}}$ and ${}^{\mathbf{C3}}\boldsymbol{R}_{\mathbf{W1}}$ are given by

$$ {}^{\mathrm{C2}}\boldsymbol{R}_{\mathbf{W1}} = \begin{bmatrix} 0.9998 & -0.0197 & -0.0012 \\ 0.0197 & 0.9997 & 0.0160 \\ 0.0008 & -0.0161 & 0.9999 \end{bmatrix} $$

$$ {}^{\mathrm{C3}}\boldsymbol{R}_{\mathbf{W1}} = \begin{bmatrix} 0.9997 & 0.0166 & -0.0200 \\ -0.0166 & 0.9999 & 0.0031 \\ 0.0201 & -0.0028 & 0.9998 \end{bmatrix}. $$

To validate the effect of the calibration method, a set of experiments are conducted by using a standard metal cylinder. The posture of the standard cylinder can be either characterized by its side-edge contour line or the normal vector of its upper surface. Since the standard cylinder's side edge contour is perpendicular to the upper surface, the former posture, denoted as $(\varphi_{x1}, \varphi_{y1})$ and obtained from the images of the side- and front-view systems by detecting the side edge contour is employed to validate the posture determined by the spatial coordinates of the three points on the upper surface using the top-view system and **LTMI**. For the sake of comparison, the latter kind of posture is also divided into two forms denoted as $(\varphi x1^*, \varphi y1^*)$ and $(\varphi' x1, \varphi' y1)$ by whether using the rotation matrix ${}^{\mathbf{C2}}\boldsymbol{R}_{\mathbf{W1}}$ and ${}^{\mathbf{C3}}\boldsymbol{R}_{\mathbf{W1}}$ or not.

In the verification experiments, 133 measurement experiments for the posture of the standard cylinder are carried out. Fig. 7(a) shows the contrast measurement results between $\varphi\prime_{x1}$ and φ_{x1} while Fig. 7(b) gives the results between φ^*_{x1} and φ_{x1}. It can be seen that with the use of rotation matrix $\mathbf{C3}_{\boldsymbol{R}_{\mathbf{W1}}}$, φ^*_{x1} is more consistent with φ_{x1} compared to φ'_{x1}. Furthermore, as Fig. 7(c) shows, the attitude error $\Delta\varphi^*_{x1} = \varphi^*_{x1} - \varphi_{\mathrm{x1}}$, distributed in the interval $[-0.25°, 0.25°]$, is improved compared to the attitude error $\Delta\varphi'_{x1} = \varphi'_{x1} - \varphi_{\mathrm{x1}}$, which is distributed in $[-0.05°, 0.40°]$. The results mentioned earlier prove that the proposed method can evaluate the posture accurately.

The achievable measurement accuracy of ***A***'s attitude may be affected by three factors: motion errors of $\mathbf{W_1}$, measurement error of **LTMI** and calibration error of rotation matrices ${}^{\mathbf{C2}}\boldsymbol{R}_{\mathbf{W1}}$ and ${}^{\mathbf{C3}}\boldsymbol{R}_{\mathbf{W1}}$. The first two kinds of errors would induce measurement error of spatial coordinates. Without considering the calibration error, (3) is employed to quantify the impact of these two kinds of errors on attitude measurement. For example, in an experiment, the coordinates of P_1, P_2, and P_3 are attained as (59.432 mm, −45.517 mm, −30.458 mm), (57.307 mm, −43.392 mm, −30.461 mm), and (55.182 mm, −45.517 mm, −30.318 mm). When the measurement error of $x_{\mathrm{W1}-n}$ with 1 μm is arisen from the motion error of x-axis, the measurement errors of φ_x and φ_y are no more than 0.001°. Similarly, the measurement error of **LTMI** with 1 μm would result in the posture error of about 0.013°. Since the repeatable accuracy of the motion platform and the measurement accuracy of **LTMI** are 0.3 and 1 μm, respectively, the first two types of errors are not the main factors affecting the measurement accuracy of the posture. Therefore, the calibration errors of rotation matrices ${}^{\mathbf{C2}}\boldsymbol{R}_{\mathbf{W1}}$ and ${}^{\mathbf{C3}}\boldsymbol{R}_{\mathbf{W1}}$, arisen from the image processing in the process of acquiring the m sets of scene points, is mainly responsible for the measurement accuracy of the posture. However, the above verification experiments show that the achievable measurement accuracy is reasonable and can meet the needs of assembly.

B. Automated Microassembly Experiment Results

1) Stage I: Attitude Control Based on Multiple Microscopic Visions: According to the automated assembly flowchart shown

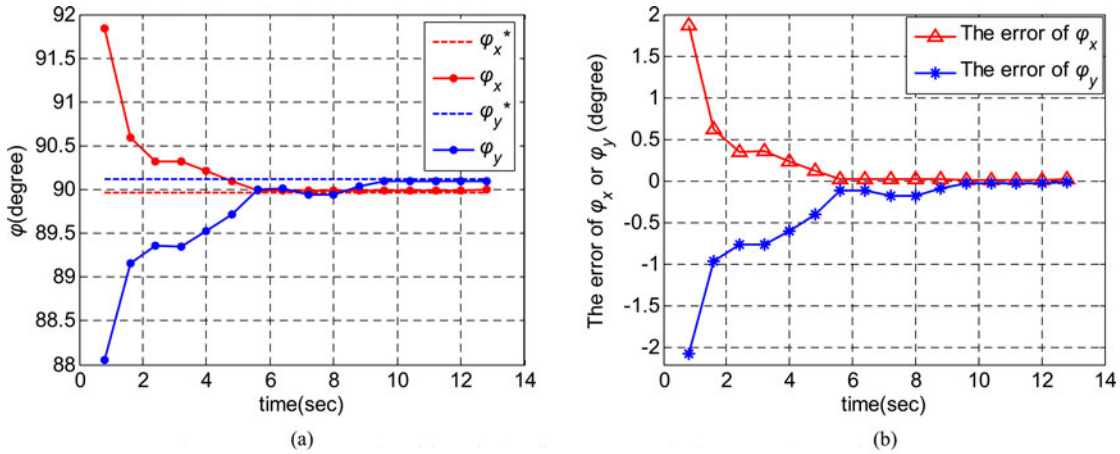

Fig. 10. Experiment results of the attitude adjustment: (a) attitudes curve; (b) attitudes' error curve.

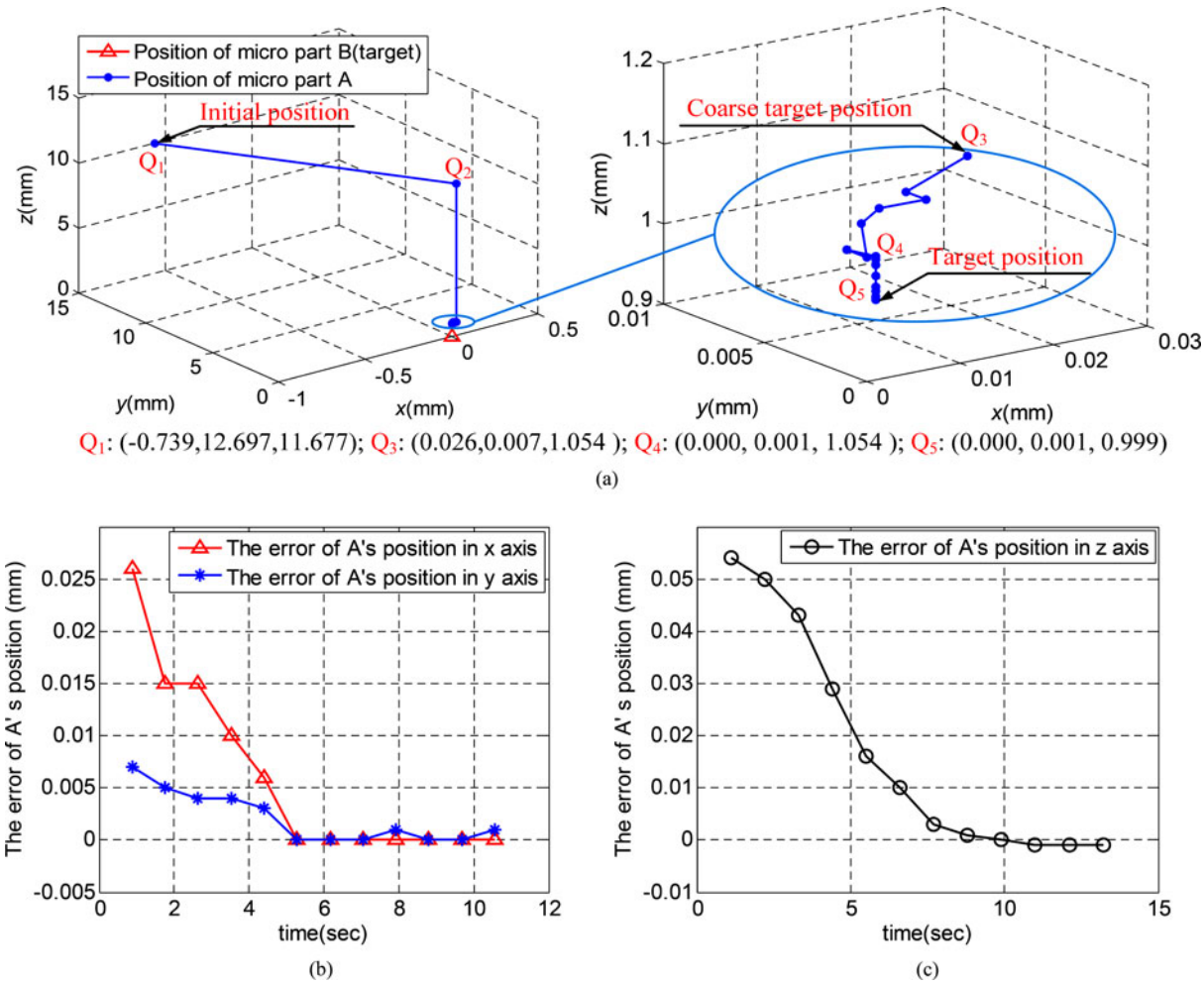

Fig. 11. Experiment results of coarse-to-fine alignment: (a) the path of $\boldsymbol{A}$; (b) center position error curve; (c) depth error curve.

in Fig. 4(b), $\boldsymbol{A}$ and $\boldsymbol{B}$ are first brought into their own initial position. Fig. 8 illustrates the process of the automated assembly. At the beginning of Stage I, as shown in Fig. 8(a), the z-axis of $\mathbf{W_1}$ is translated to let the top-view system focus on $\boldsymbol{A}$, thus, the clear image of $\boldsymbol{A}$ is attained as shown in Fig. 9(a). After some image processing, the coordinate of the inner circle center is obtained and utilized to guide the **LTMI** to measure the depth of $P_1 - P_3$ on the upper surface of $\boldsymbol{A}$, as shown in Fig. 8(b). Using the method proposed in Section III, the attitudes of $\boldsymbol{A}$ (φ_x^*, φ_y^*) represented in $\boldsymbol{o_{I2}u_{I2}v_{I2}}$ and $\boldsymbol{o_{I3}u_{I3}v_{I3}}$ are obtained. The

entire attitude measurement process for $\boldsymbol{A}$ generally requires an average of 53 s, much of which are consuming in the guiding process of **LTMI**.

In the process of attitude measurement of $\boldsymbol{A}$, regarding $\boldsymbol{A}$'s attitude as target, the attitude controller presented in Section IV is then employed to adjust $\boldsymbol{B}$'s attitude by rotating the axis θ_x and θ_y of $\mathbf{W_5}$. Note that the attitude measurement experiment of $\boldsymbol{B}$ shows that the accuracy of φ_x and φ_y is about 0.2°. From the attitudes curve and attitudes error curve shown in Fig. 10, the designed attitude controller had reached the performance of confining attitude error within 0.3°. The average time required for the attitude adjustment is about 13 s. Therefore, after the attitude errors had been adjusted within specified range for five control periods continuously, the assembly process automatically jumps into the stage of coarse-to-fine alignment control.

2) Stage II: Coarse-to-Fine Alignment Control: According to the coarse-to-fine control strategy presented in Section IV, the spatial coordinate $(x_{\mathrm{W}1-B}, y_{\mathrm{W}1-B}, z_{\mathrm{W}1-B})$ of $\boldsymbol{B}$ needs to be measured at first and the time consuming in the part is about 58 s. Fig. 9(b) shows the clear image of the $\boldsymbol{B}$'s counterbore using the top-view system. Fig. 11(a) shows the path of $\boldsymbol{A}$ in the process of alignment in an automated assembly experiment which is represented as the relative position to $\boldsymbol{B}$. Thus, the spatial coordinate of $\boldsymbol{B}$ is set as (0, 0, 0). Q_1, Q_3, and Q_5 are the initial position, the coarse target position, and the target position of $\boldsymbol{A}$, respectively, while Q_2 and Q_4 are the transition positions. The path from Q_1 to Q_2 in Fig. 11(a) is formed in the coarse center alignment process whose scenes are shown in Fig. 8 (c) and (d). The path from Q_2 to Q_3 in Fig. 11(a) is formed subsequently in the process of coarse control for the distance between lower surface of $\boldsymbol{A}$ and upper surface of $\boldsymbol{B}$'s counter-bore whose scenes are shown in Fig. 8 (d) to Fig. 8 (e). The average time required for the coarse alignment is about 10 s.

After the coarse alignment, the inner center of the $\boldsymbol{A}$ deviates from $\boldsymbol{B}$'s center generally about 26 μm and 7 μm in x-axis and y-axis, respectively, caused by the tiny attitude deviation existed between $\boldsymbol{o}_{\mathrm{W}1}\boldsymbol{x}_{\mathrm{W}1}\boldsymbol{y}_{\mathrm{W}1}\boldsymbol{z}_{\mathrm{W}1}$ and $\boldsymbol{o}_{\mathrm{W}4}\boldsymbol{x}_{\mathrm{W}4}\boldsymbol{y}_{\mathrm{W}4}\boldsymbol{z}_{\mathrm{W}4}$. These errors will be eliminated in the subsequent fine control. Before the fine alignment, the top-view system is moved to focus $\boldsymbol{A}$ and $\boldsymbol{B}$**.** This preparation process needs about 18 s.

As shown in Fig. 11(a), the path from Q_3 to Q_4 illustrates the process of the center fine alignment. Moreover, from the center position error curve shown in Fig. 11(b), the center fine alignment controller is proved to have good performance of controlling the center position error within 3 μm. Fig. 9(c) shows the image of $\boldsymbol{A}$ and $\boldsymbol{B}$ after center fine alignment. The average time required for this part is about 11 s. After the center position error had been controlled within 3 μm for 5 control periods continuously, the assembly process automatically jumps into the depth fine alignment.

Before the depth alignment, **LTMI** needs to be guided by the top-view system to measure the depth of the point P_2' on the upper surface of $\boldsymbol{A}$, which needs about 35 s. The path from Q_4 to Q_5 presents the process of this part as shown in Fig. 11(a). It is noted that the controller is required to be prevented from excessive overshoot since it may produce excessive contact force that would cause the changing of $\boldsymbol{A}$'s posture. As shown in Fig. 11(c), the proposed controller can meet the requirement and the error is within the range of ± 2 μm. The time required for this part is about 14 s in average. Finally, in stage III, to end the assembly $\boldsymbol{A}$'s microgripper is removed out of the $\boldsymbol{B}$'s counterbore when the $\boldsymbol{A}$ is completely glued with $\boldsymbol{B}$ as shown in Fig. 8(f). It is noted that the time required for the entire assembly process is about 276 s includes not only the measurement and adjustment time but the preparation time for the sensors as well.

TABLE I
PARAMETERS OF CONTROLLERS

Num	Controller Parameter	Control Period	Accuracy	Accuracy
1. Attitude adjustment	$K_{P1} = 0.08, K_{I1} = 0.35,$	0.8 s	0.3°	0.5°
2. Center alignment	$K_{P2} = 0.05, K_{I2=0.38},$	0.9 s	3 μm	3 μm
3. Depth alignment	$K_{\mathrm{P}3} = 0.09, K_{I3} = 0.29,$ $K_{D3} = 0.04$	1.1 s	2 μm	

To further test the performance of the automated assembly methodology, repetitive automated microassembly tasks are carried out. Sixty times assembly tasks with varying initial position and pose of $\boldsymbol{A}$ and initial pose of $\boldsymbol{B}$ are implemented, and 57 assembly attempts are successful giving a success rate of 95%. The three failed attempts are caused by the image feature matching error in measuring the center position of $\boldsymbol{A}$ in the process of fine center position alignment duo to some stains on $\boldsymbol{A}$'s surface produced by vacuum sucker among different grasping experiments. Besides, the environmental vibrations and light changes are also the potential factors leading to failure. Through these experiments the methods proposed in this paper are verified to have good performance. The average alignment accuracy and the specific parameters of controllers including coefficients and control period are given in Table I. Note that the Jacobian matrix $\boldsymbol{J}_1$ is approximated as identity matrix after calibration which implies that the axes θ_x and θ_y are substantially parallel to the axes $\boldsymbol{o}_{\mathbf{C3}}\boldsymbol{y}_{\mathbf{C3}}$ and $\boldsymbol{o}_{\mathbf{C2}}\boldsymbol{x}_{\mathbf{C2}}$, respectively. Besides, the Jacobian matrix $\boldsymbol{J}_2$ is also approximated as identity matrix after calibration.

Moreover, to test the versatility of our method, the experiment using other kinds of microparts are carried out. Other shapes of micropart such as a metal cylinder and a cuboid are used to prove the versatility of the attitude measurement method. The results of the attitude measurement experiment show that the accuracy of about 0.3° is achieved. Meanwhile, the assembly experiment for a micropeg and a microhole is carried out to verify our control strategy. The microhole is made of aluminum with a diameter of 5 mm and a thickness of about 1 mm. There is a mechanical clearance of about 60 μm between the peg and hole. Thirty times assembly tasks with varying initial position and pose are implemented, and 29 assembly attempts are successful, giving a success rate of 96.7%. The results of the experiment verify the versatility of our method. However, it should be noted that our attitude measurement is not suitable for measuring the transparent micropart due to the depth measurement using **LTMI** will be affected because of the laser full penetration.

In summary, the microassembly task in this paper involves both measurement and control for the position and attitudes

of the microparts. Thus, the assembly errors are produced inevitably including the measurement errors and control errors which are due to the calibration error, precision of motion platform, image processing, measurement error of LTMI and the environmental disturbance. Nevertheless, the error curves of attitude and position obtained in the experiments have demonstrated that the proposed method can well meet the requirements with the following accuracy: 3 μm for the center position error, 2 μm for the depth error, and 0.3° for the attitude error.

VI. Conclusion

A fully automated assembly methodology of a slice micropart in 3-D space with the requirement of attitude adjustment is studied through this paper. An automated measurement method based on **LTMI** guided by microscopic vision is proposed to acquire the attitude of the slice micropart since it cannot be accurately obtained simply based on microscopic image due to its lower depth of field. Meanwhile, an accurate calibration method for telecentric vision system is presented to perform calibrated measurement frames. To achieve the automated assembly with a high precision in 3-D space, we proposed a three-stage control strategy, including attitude adjustment control based on multi-microscopic visions and coarse-to-fine alignment control based on **LTMI** and microscopic vision. Experiments conducted on the microassembly robot demonstrate the effectiveness of the proposed method and the assembly tasks were performed with the following accuracy: 3 μm for the center position error, 2 μm for the depth error, and 0.3° for the attitude error. Future work will concern the further efficiency improvement of the proposed assembly methodology by optimizing the path of assembly. It would also be interesting to assemble other shape of microparts with shrink fit requirement based on microscopic vision and microforce.

Acknowledgment

The authors would like to thank G. Liu, B. Liu, F. Wan, and W. Wang who are with the Department of Automatic Measurement and Control, Harbin Institute of Technology, Harbin, China, for their work on the development of microscopic vision detection system.

References

[1] H. Van Brussel, J. Peirs, D. Reynaerts, A. Delchambre, G. Reinhart, N. Roth, M. Weck, and E. Zussman, "Assembly of microsystems," *CIRP Ann. Manuf. Technol.*, vol. 49, no. 2, pp. 451–472, 2000.

[2] J. Fluitman, "Microsystems technology: Objectives," *Sens. Actuators A Phys.*, vol. 56, pp. 151–166, 1996.

[3] J. Cecil, D. Powell, and D. Vasquez, "Assembly and manipulation of micro devices—A state of the art survey," *Robot. Compu.-Integ. Manuf.*, vol. 23, pp. 580–588, 2007.

[4] D. O. Popa and H. E. Stephanou, "Micro and mesoscale robotic assembly," *J. Manuf. Proc.*, vol. 6, no. 1, pp. 52–71, 2004.

[5] L. Wang, L. Ren, J. K. Mills, and W. L. Cleghorn, "Automated 3-D micrograsping tasks performed by vision-based control," *IEEE Trans. Autom. Sci. Eng.*, vol. 7, no. 3, pp. 417–426, Jul. 2010.

[6] Y. Sun, S. Duthaler, and B. J. Nelson, "Autofocusing algorithm selection in computer microscopy," in *Proc. IEEE IROS*, Alberta, QC, Canada, 2005, pp. 70–76.

[7] S. J. Ralis, B. Vikramaditya, and B. J. Nelson, "Micropositioning of a weakly calibrated microassembly system using coarse-to-fine visual servoing strategies," *IEEE Trans. Electron. Packag. Manuf.*, vol. 23, no. 2, pp. 123–131, Apr. 2000.

[8] A. Buerkle and S. Fatikow, "Laser-measuring system for a flexible microrobot-based micro-manipulation station," in *Proc. IEEE IROS*, Takamatsu, Japan, 2000, pp. 799–804.

[9] T. Sano and H. Yamamoto, "Study of micro-manipulation using stereoscopic microscope," *IEEE Trans. Instrum. Measur.*, vol. 51, no. 2, 182–187, Apr. 2002.

[10] J. Sulzer and I. Kovac, "Enhancement of positioning accuracy of industrial robots with a reconfigurable fine-positioning module," *Precis. Eng.*, vol. 34, pp. 201–217, 2010.

[11] F. Li, D. Xu, Y. Shi, and Z. Zhang, "Pose measuring and aligning of a glass tube and a hole on the sphere," *High Tech. Lett.*, vol. 24, no. 4, pp. 401–406, 2014.

[12] B. Tamadazte, E. Marchand, S. Dembele, and N. L. F. Piat, "CAD model based tracking and 3D visual-based control for MEMS micro-assembly," *Int. J. Robot. Res.*, vol. 29, no. 11, pp. 1416–1434, 2010.

[13] L. Ma, W. Rong, and L. Sun, "Multi-sensor control for precise assembly of optical components," *Chin. J. Aeronaut.*, vol. 27, no. 3, pp. 613–621, 2014.

[14] J. Salvi, X. Armangu, and J. Batlle, "A comparative review of camera calibrating methods with accuracy evaluation," *Pattern Recognit.*, vol. 35, pp. 1617–1635, 2002.

[15] L. Wang, J. K. Mills, and W. L. Cleghorn, "Automatic micro-assembly using visual servo control," *IEEE Trans. Electron. Packag. Manuf.*, vol. 31, no. 4, pp. 316–325, Oct. 2008.

[16] B. Tamadazte, N. L. F. Piat, and S. Dembele, "Robotic micro-manipulation and micro-assembly using monoview and multiscale visual servoing," *IEEE Trans. Mechatron.*, vol. 16, no. 2, pp. 277–287, Apr. 2011.

[17] B. Tamadazte, N. L. F. Piat, S. Dembele, and E. Marchand, "Micro-assembly of complex and solid 3D MEMS by 3D vision-based control," in *Proc. IEEE IROS*, St. Louis, MI, USA, 2009, pp. 3284–3289.

[18] A. Ferreira, C. Cassier, and S. Hirai, "Automatic micro-assembly system assisted by vision servoing and virtual reality," *IEEE Trans. Mechatron.*, vol. 9, no. 2, pp. 321–333, Jun. 2004.

[19] E. T. Enikov, L. L. Minkov, and S. Clark, "Micro-assembly experiments with transparent electrostatic gripper under optical and vision-based control," *IEEE Trans. Ind. Electron.*, vol. 52, no. 4, pp. 1005–1012, Aug. 2005.

[20] D. Lee, M. Kim, and H. Cho, "Path planning for micro-part assembly by using active stereo vision with a rotational mirror," *Sens. Actuators A Phys.*, vol. 193, pp. 201–212, 2013.

[21] D. Li and J. Tian, "An accurate calibration method for a camera with telecentric lenses," *Opt. Lasers Eng.*, vol. 51, pp. 538–541, 2013.

[22] J. Heikkila and O. Silven, "A four-step camera calibration procedure with implicit image correction," in *Proc. IEEE CVPR*, San Juan, Puerto Rico, 1997, pp. 1106–1112.

[23] J. More, "The Levenberg–Marquardt algorithm, Implementation and theory," in *Numerical Analysis, Lecture Notes in Mathematics*, vol. 630, G. A. Watson, Ed. New York, NY, USA: Springer-Verlag, 1977, pp. 105–116.

[24] J. Zhang, D. Xu, Z. Zhang, and L. Luo, "An automatic alignment strategy of micro parts based on microscope vision systems," *Robot*, vol. 36, no. 1, pp. 69–75, 2014.

Fei Shen received the B.S. degree in measurement and control technology and instrument from Xidian University, Xi'an, China, in 2007, the M.S. degree in navigation, guidance, and control from Beijing Institute of Technology, Beijing, China, in 2009, and the Ph.D. degree in control science and engineering from Institute of Automation, Chinese Academy of Sciences (IACAS), Beijing, China, in 2012.

He is currently a Postdoctoral Researcher at the Laser Fusion Research Center, Mianyang, China, and an Assistant Professor in the Research Center of Precision Sensing and Control, IACAS. His current research interests include robot control, robot vision control, and microassembly.

Wenrong Wu received the B.S. degree in mechanical design and manufacturing from Chongqing University, Chongqing, China, in 2000, and the M.S. degree in mechanical and electrical engineering from the University of Electronic Science and Technology, Chengdu, China, in 2006.

He is currently a Vice Professor at the Laser Fusion Research Center and Laboratory of Precision Manufacturing Technology, Chinese Academy of Engineering Physics (CAEP), Mianyang, China. His current research interests include design of electromechanical integration, especially the control of microassembly robot.

Dahai Yu received the M.S. degree in mechanical and electrical engineering from Chongqing University, Chongqing, China, in 2005 and 2009.

He is currently an Assistant Professor at the Laser Fusion Research Center and Laboratory of Precision Manufacturing Technology, Chinese Academy of Engineering Physics (CAEP), Mianyang, China. His current research interests include design of electromechanical integration, especially the design and finite element analysis method of microgripper.

De Xu (M'05–SM'09) received the B.S. and M.S. degrees from Shandong University of Technology, Jinan, China, in 1985 and 1990, respectively, and the Ph.D. degree from Zhejiang University, Hangzhou, China, in 2001, all in control science and engineering.

Since 2001, he has been with the Institute of Automation, Chinese Academy of Sciences (IACAS), Beijing, China, where he is currently a Professor at the Research Center of Precision Sensing and Control. His current research interests include robotics and automation, in particular, the control of robots, such as visual control and intelligent control.

Zhiqiang Cao (M'08–SM'14) received the B.S. and the M.S. degrees from the Shandong University of Technology, Jinan, China, in 1996 and 1999, respectively, and the Ph.D. degree in control theory and control engineering from the Institute of Automation, Chinese Academy of Sciences (IACAS), Beijing, China, in 2002.

He is currently a Vice Professor in the State Key Laboratory of Management and Control for Complex Systems, IACAS. His current research interests include robots and intelligent control.